THESIS FOR THE DEGREE OF DEGREE OF DOCTOR OF PHILOSOPHY IN THERMO
AND FLUID DYNAMICS

Investigation of tonal noise sources from centrifugal fan using detached eddy simulation

MARTIN OTTERSTEN

Department of Mechanics and Maritime Science

CHALMERS UNIVERSITY OF TECHNOLOGY

Gothenburg, Sweden 2022

Investigation of tonal noise sources from centrifugal fan using detached eddy simulation
MARTIN OTTERSTEN
Department of Mechanics and Maritime Science
Chalmers University of Technology

Abstract

Since we spend the majority of our time indoors, heating, ventilation, and air conditioning (HVAC) systems have become a more and more important part of many people´s life. They provide a sufficient amount of airflow with the correct temperature, quality, and humidity. The negative side is the noise it produces and the dominant one is the tonal noise which is generated by the fan. In the fan, there is a gap between the rotating shroud and the stationary inlet duct. The pressure difference between the fan's inner and outer sides drives air to pass through the gap.

In this thesis, tonal noises at the blade passing frequency (BPF) produced by a centrifugal fan is investigated to be able to understand the generation mechanism and identify their sources. The approach is to use the hybrid method coupling the improved delayed detached eddy simulation with Formulation 1A of Farassat.

In part one, it is found that recirculating flows at the blades are associated with the gap between the shroud and the inlet duct. The turbulence that develops at the gap is swept along the shroud wall and is swept downstream to interact with the top side of the blade leading edge (BLE). The interaction renders uneven surface pressure distributions among the blades that agree with the tonal noise sources from the wall-pressure fluctuations.

In part two, different gap geometries are studied and it is found that the gap designs affect the amplitude of the root mean square (RMS) pressure on the BLE. The Spectral analysis shows that the regions with high energy correspond to the high RMS regions at the BLE and that the amplitude of the tonal noise at the BPF differs between the cases.
Also, the turbulent structures at the gap are swept downstream along the intersection between the blade and shroud, on the pressure side of the blade. They render unevenly high-pressure regions in the blade passage. The high-pressure regions rotate with a speed of approximately 5 % of the fan rotation speed.

Keywords: Computational Aeroacoustics, Tonal Noise, Blade Passing Frequency, Centrifugal Fan, low-frequency rotation.

Acknowledgments

List of abbreviations

Thesis

This thesis consists of an extended summary and the following appended papers:

Paper I M. Ottersten, H.-D. Yao, and L. Davidson, "Unsteady Simulation of tonal noise from isolated centrifugal fan," *Conference paper FAN2018*. Darmstadt, Germany, (2018)

Paper II M. Ottersten, H.-D. Yao, and L. Davidson, "Tonal noise of voluteless centrifugal fan generated by turbulence stemming from upstream inlet gap," Phys. Fluids, 33, (2021). https://doi.org/10.1063/5.0055242. (Editor´s pick).

Paper III M. Ottersten, H.-D. Yao, and L. Davidson, "Inlet gap effect on tonal noise generated from a voluteless centrifugal fan," Conference paper FAN2022. Senlis, France, (2022)

Paper IV M. Ottersten, H.-D. Yao, and L. Davidson, "Inlet gap effect on aerodynamics and tonal noise generated from a voluteless centrifugal fan," Reviewed, positive with minor revision, Journal of Sound and Vibrations, (2022)

Paper V M. Ottersten, H.-D. Yao, and L. Davidson, "Inlet gap influence on low-frequency rotation in a centrifugal fan at high mass flow," Submitted to a scientific journal, (2022)

Paper VI M. Ottersten, H.-D. Yao, and L. Davidson, "Effect of micro vortex generators on tonal noise from a centrifugal fan," Submitted to conference, abstract accepted, ICA2022 (2022)

Other publications

Paper VII M. Ottersten, H.-D. Yao, and L. Davidson, "Numerical and experimental study of tonal noise sources at the outlet of an isolated centrifugal fan," (2020) arXiv:2011.13645.

Patent A M. Ottersten, Inventors; Swegon AB, applicant. "Fan for Air Handling Unit – Increasing efficiency," *Submitted*, (2019)

Patent B M. Ottersten, Inventors; Swegon AB, applicant. "Fan for Air Handling Unit – Increase strength," International patent WO 2021034260, (2021)

Patent C M. Ottersten, Inventors; Swegon AB, applicant. "Accessory to Fan for Air Handling Unit – Increase efficiency and decreases noise," International patent WO *2021194409*, (2021)

Patent D   M. Ottersten, Inventors; Swegon AB, applicant. "Fan for Air Handling Unit – Decrease Tonal Noise at BPF," *Submitted*, (2022)

Content

1 Introduction

1.1 Background

Today most people spend the majority of their time indoors, up to 90 % [1]. The indoor environmental quality (IEQ) has become more and more important. When considering IEQ we usually think about temperature, CO_2 level, and humidity. However, it has been established that sound quality is also an important factor for high-quality IEQ [2, 3]. Noise is harmful to human's health not only by directly causing loss of hearing and tinnitus but also by indirectly producing annoyance, sleep disturbance, and stress [4]. All of these will affect performance and well-being. It was reported in [5] that noise has a detrimental effect on reading and writing and that the cognitive development in children is affected by chronic exposure to noise.

The structure of modern buildings is good at reducing external noise from traffic, and significant improvements have been made over recent years [6]. Although the internal noise from heating, ventilation, and air conditioning (HVAC) systems is difficult to isolate, low-speed centrifugal fans installed in the HVAC systems are known as dominant noise contributors. The frequency of the tonal noise is connected to the rotation speed of the fan. In variable air volume (VAV) systems the fan speed changes continuously to meet the demand. It means that the tonal noise changes continuously over a wide range of frequencies. The noise can be reduced by placing silencers in ducts, but the silencers introduce additional pressure loss. Besides, the silencers are mainly effective in absorbing broadband noise rather than tonal noise. They can be tuned to damp the tonal noise at specific frequencies, while the tuning is not valid for a wide range of frequencies [7].

Nowadays a ventilation system is usually driven by voluteless centrifugal fans. These are fans where the volute (spiral casing surrounding the fan) is removed, termed voluteless in this study. Regarding the structure of the rotor part, a shroud and a backplate are assembled onto the top and bottom sides of the rotating blades, respectively. The fan tonal noise generation is attributed to multiple causes. Pressure and density fluctuations on fan blades are identified as dominant sources in a large body of studies, e.g., by Ffowcs Williams and Hawkings [8]. As found in both simulations and experiments for voluteless fans [9], the tonal noise at the blade passing frequency (BPF) is generated from a helical unsteady inlet vortex that interacts with the rotating blades near the fan backplate. Another cause is inflow distortion, which leads to flow separation at the blade root near the backplate [10]. Based on this finding, flow obstructions were proposed upstream of the fan inlet [11]. The shape and location of the

obstructions were identified as the key parameters for noise reduction. As the present study focuses on tonal noise, broadband noise sources (e.g., see Ref [12]) are not reviewed.

In an HVAC voluteless centrifugal fan, there is a gap (also termed clearance) between the rotating fan shroud and the stationary inlet duct, see figure 1. The pressure difference between the fan's inner and outer sides drives air to pass through the gap. As clarified by Hariharan and Govardhan [13], increasing the gap width worsens the blade aerodynamic performance. According to Lee [14], the gap gives rise to a local jet that aggravates flow separation near the front shroud. This finding was further proven in later studies [15], where the visualization of streamlines indicates that the flow discharged from the gap creates recirculating flow around the intersection of the front shroud and the blade trailing edge (BTE). As demonstrated in experiments [16, 17], the curved shape of the shroud also accounts for the flow separation. It is worth noting that the shroud skin friction leads to extra rotational momentum near the shroud walls. The same finding was also reported in [18]. This effect is different from conventional blade vortex interaction (e.g., [19]), where the flow upstream of the blades is quiescent.

The noise from voluteless centrifugal fans was numerically studied by Schaeffer and Boehle [20]. It was found that the accuracy of the noise prediction, especially at BPF, is improved when the mesh is refined at the gap and the fan outlet. But this study provided few discussions on the physical mechanisms that are associated with the improved accuracy.

1.2 The beginning

Tonal noise at the BPF is a well-known problem for ventilation manufactories. It impacts the indoor environment quality which in the end affects people's health. The sound pressure level (SPL) measured in an experimental rig for one of Swegon´s centrifugal fans is shown in Figure 1. It is obvious that the BPF and its harmonics affect the IEQ. Requirements in buildings are given in 1/3 octave bands, unfortunately, this hides the tonal noise in some cases, see Figure 1.
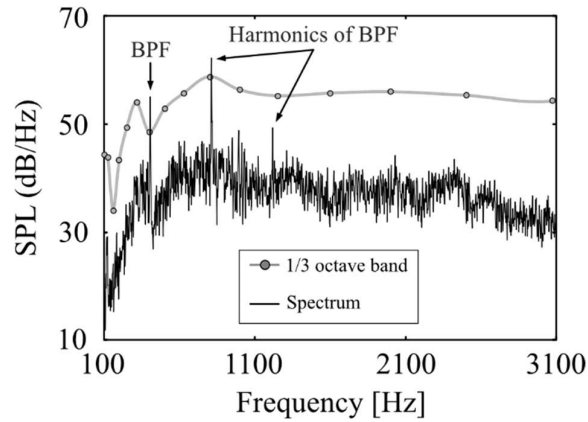
Figure 1. SPL of the sound downstream of the fan.

One of the first study on a voluteless fan was performed by Wolfram and Carolus [9]. They reported that the tonal noise at the *BPF* is generated from a helical unsteady inlet vortex that interacts with the rotating blades near the fan backplate, shown in Figure 2.
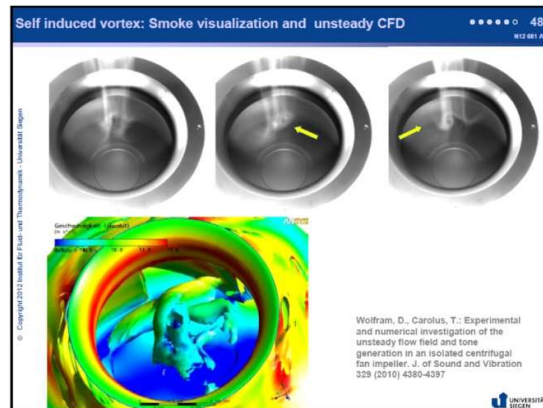

Figure 2. D. Wolfram and T. Carolus "Experimental and numerical investigation of the unsteady flow field and tone generation in an isolated centrifugal fan impeller".

Three different cases were tested at Swegon to investigate the vortex near the backplate, they are illustrated in Figure 3. A flow straightening structure (also termed honeycomb (HC) colored brown) was assembled before the inlet duct, to straighten the inlet flow. A vortex-affecter was placed inside the fan in Cases B and C to affect the helical unsteady inlet vortex. For Case C it was flipped and moved away from the backplate so that the largest diameter is at the location of the gap. The three cases are described in Table 1. The sound pressure level for the three cases is shown in Figure 4. The amplitude of the tonal noise at the *BPF* is decreased for Case C, compared to Case A and for Case B it is almost the same. The author

3

thought that something else than the helical unsteady inlet vortex has to interact with the blades. These results motivated the author to do this thesis.
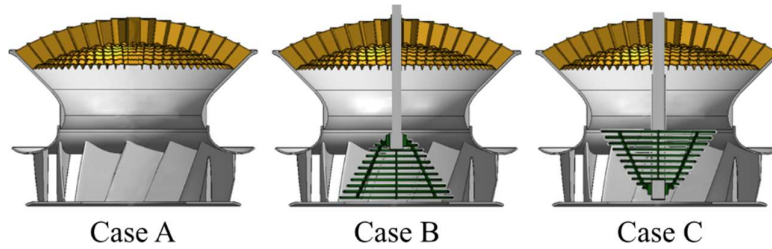
Figure 3. Geometry setup, honeycomb colored brown and vortex-affecter colored green.

Table 1. Description of the cases

	HC before the inlet duct	Vortex-affecter
Case A (reference)	Yes	-
Case B	Yes	Yes
Case C	Yes	Yes, flipped and moved
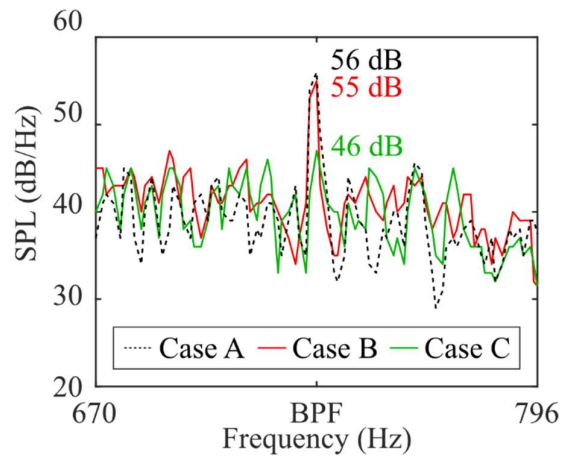
Figure 4. Sound pressure level for Case A, B, and C at the BPF.

1.3 The HVAC system

One of the functions of HVAC systems is to control the temperature, the quality, and the humidity in the airflow. An air handling unit (AHU) is designated for the controlling. It moves and cleans air, as well as recovers latent and sensible heat in the air. As illustrated in Figure 5, a modern AHU usually consists of a fan, a filter, and two channels such as a supply and an extract. The fan is of the centrifugal type running at low speeds, to satisfy the

requirements on small size and high pressure airflow [21]. The turbulent flow induced by the rotating fan emits noise in buildings [22]. The noise has both broadband and tonal parts.

Figure 5. Swegon´s AHU - Gold 12 RX.

1.4 Application case - Centrifugal fan

The tonal noise in an AHU is mainly produced by the fan component. Therefore, the present study is organized to specifically inves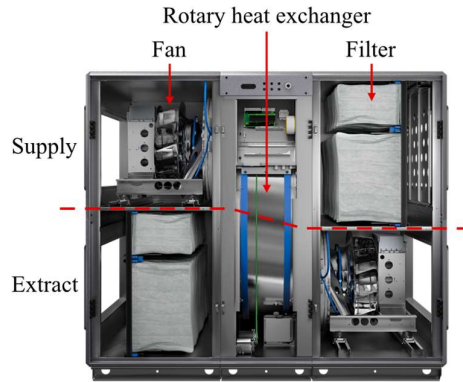tigate an isolated fan, i.e. without the AHU. A AHU is usually driven by voluteless low-speed centrifugal fans. These are fans where the volute (spiral casing surrounding the fan) is removed, termed voluteless in this study.

The numerical setup for the fan is illustrated in Figure 6. There are two ducts, which are placed upstream and downstream of the fan. The flow at the inlet is undisturbed with a uniform velocity profile. There is a gap (colored blue) between the rotating fan shroud and the stationary inlet duct. The pressure difference between the fan's inner and outer sides drives air to pass through the gap. As displayed in Figure 6 a, the fan and inlet duct is placed in a downstream duct, and the inlet duct is connected to an upstream duct. This simple geometry layout is designed for the numerical simulations. This simplification reduces the geometry complexity but retains the principal flow and acoustic characteristics. The fan parameters are listed in Table 1 and the gap width ,w, in Table 2.
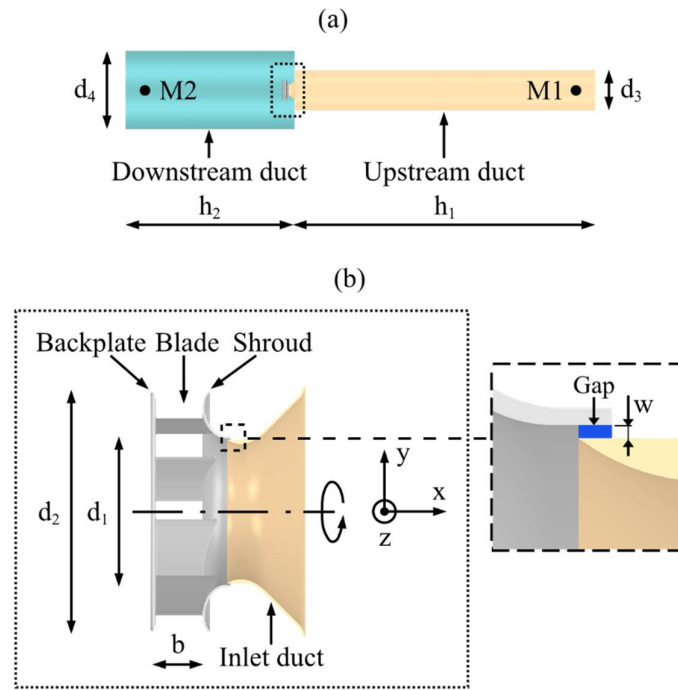
Figure 6. a) The simple geometry layout for the numerical simulations. b) The fan configuration and inlet duct. The gap is colored blue. The rotation axis of the fan is the x-axis.

Table 1. The fan parameters.

d_1	d_2	d_3	d_4	b	h_1	h_2
0.165 m	0.268 m	0.6 m	1.1 m	0.053 m	4.0 m	2.3 m

Different gap geometries and designs are studied in Paper III (Cases 1, 2, and 3) and in Paper IV (Cases 1, 2, 3, and 4). The baseline fan (Case 1) and the three different designs (Case 2, Case 3, and Case 4) are illustrated in Figure 7. Case 1 is the same fan as the one examined in Paper I, II, V. The fan backplate and blades are the same for all cases and there are seven blades. For Cases 1, 2, and 3 the shroud geometry is the same, and the flow path of the gap is straight in the streamwise direction. Case 2 has larger gap width (denoted by w), and Case 3 has smaller one than Case 1. The gap width is varied by changing the wall thickness of the inlet duct. In comparison to the other cases, a curved flow path of the gap is designed for Case 4, while its gap width is the same as Case 1. The gap width in Table 2.
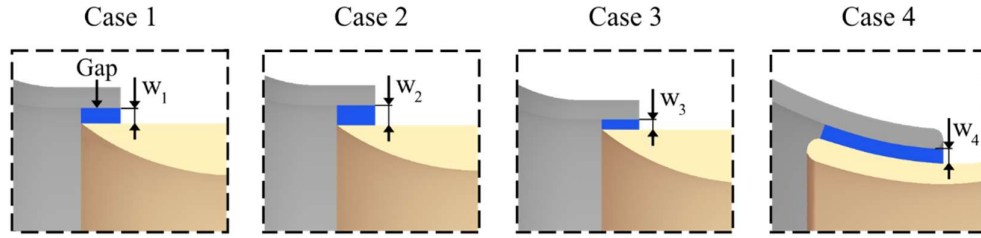
6

Figure 7. Case 1 (baseline), Case 2 (larger gap width), Case 3 (smaller gap width), and Case 4 (curved gap, same gap width)

Table 2. The gap width.

w_1	w_2	w_3	w_4
1.5 mm	2.0 mm	1.0 mm	1.5 mm

1.5 Operation point

The fan rotation speed is 2800 rpm (revolutions per minute). Given that the fan has 7 blades, the blade passing frequency BPF is 326.7 Hz, and the first harmonic frequency 653.4 Hz.

The fan characteristic curve is shown in Figure 8a. Five operation points are measured. The maximum efficiency point is found between Points 2 and 3, where the pressure rise is 410.83 Pa and the mass flow rate is 0.36 kg/s. The power spectral density (PSD) of the tonal noise at the BPF is shown in Figure 8b. The noise increases at the off-design condition Point 4, where the pressure rise is 269.65 Pa and the mass flow rate is 0.467 kg/s. Hence, Point 4 is specifically studied to understand the causes of the noise increase.
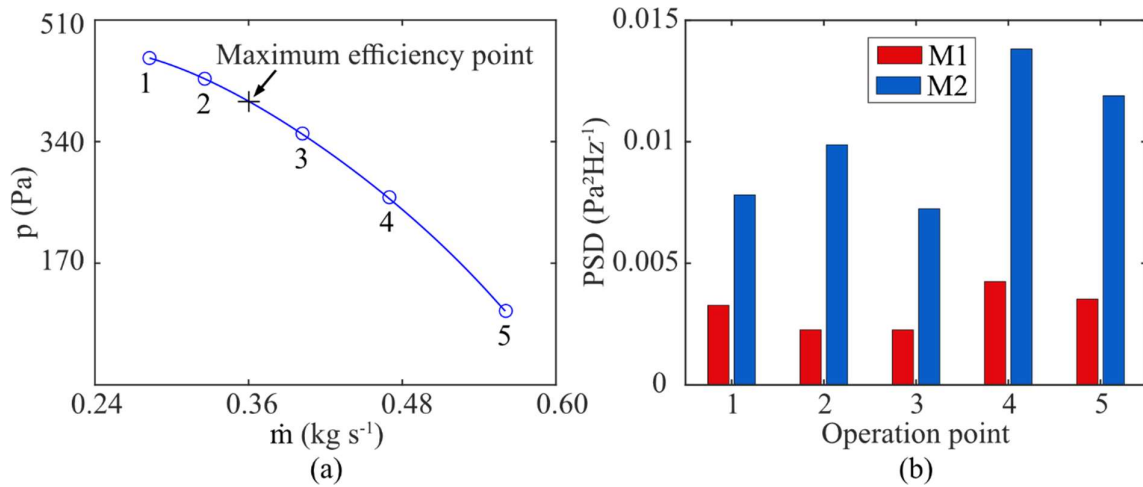

Figure 8. a) The fan characteristic curve at the fan rotation speed of 2800 rpm. The operation points labeled with circles are further measured for the tonal noise. b) The PSD of the tonal noise at the blade passing frequency BPF for the upstream microphone (M1) and the downstream microphone (M2).

1.6 Aim

This study is aimed at developing a hybrid computational aeroacoustics (CAA) method to accurately predict the fan tonal noise, in particular, at BPF. The mechanisms of the tonal noise generation will be explored and the noise sources will be identified. Moreover, different fan geometries will be studied to investigate if the amplitude of the BPF can be decreased. The hybrid CAA method couples a computational fluid dynamics (CFD) method with the Ffowcs Williams and Hawkings (FW-H) acoustic analogy. The CFD method are the improved delayed detached eddy simulation (IDDES). Formulation 1A of the FW-H acoustic analogy is chosen. The CAA method will be validated based on experiments.

2 Methods

Understanding and predicting tonal noise is not easy since the noise has much lower energy than the flow. A convenient method is to use acoustic analogy. The acoustic analogy was first proposed by Lighthill [23]. The basic principle of the acoustic analogy is to separate the computation of the noise generation and propagation from the flow simulation. The theory has been developed into a family of methods, in which the FW-H analogy is the most popular one. In this study, a hybrid approach coupling various CFD methods with the FW-H analogy is employed. The unsteady flow field is simulated using Improved Delayed Detached Eddy Simulation (IDDES) [24]. The FW-H analogy is implemented with Formulation 1A [25].

The air is considered as an ideal gas. The flow is compressible. A finite volume method is utilized to discretize the continuity, momentum, and energy equations. The method employs a segregated flow solver accomplished with the Semi-Implicit Method for Pressure-Linked Equations (SIMPLE) algorithm [26].

The convection flux on a cell face is discretized utilizing a hybrid second-order upwind and bounded scheme. The diffusion fluxes on both internal and boundary cell faces are discretized with a second-order scheme. The second-order hybrid Gauss-LSQ method is used in gradient computation. A second-order implicit method is taken to discretize the time derivative. The time marching procedure adopts inner iterations at every preconditioned pseudo-time step. All simulations are performed using the commercial software STAR-CCM+ [24]. This setup was validated in the previous study [27], where turbulence-induced acoustic waves transmitting through a cabin window were simulated.

2.1 Governing equations

The transport equations of continuity, momentum, and energy equations in the conservation form, which are solved by CFD solvers, are generally written as

$$\frac{\partial \rho}{\partial t} + \nabla \cdot (\rho \boldsymbol{u}) = 0,$$

$$\frac{\partial (\rho \boldsymbol{u})}{\partial t} + \nabla \cdot (\rho \boldsymbol{u} \otimes \boldsymbol{u}) = -\nabla p + \nabla \cdot \boldsymbol{\tau},$$

$$\frac{\partial}{\partial t}(\rho E) + \nabla \cdot (\rho E \boldsymbol{u}) = \nabla \cdot (k \nabla T) - \nabla \cdot (\rho \cdot \boldsymbol{u}) + \nabla \cdot (\boldsymbol{u} \cdot \boldsymbol{\tau}) \qquad (1)$$

where the total energy $E = e + \boldsymbol{u} \cdot \boldsymbol{u}/2$, and e is the internal energy.

If the compressibility is taken into account, the viscous stress tensor $\boldsymbol{\tau}$ is defined as

9

$$\boldsymbol{\tau} = \mu[\nabla u + (\nabla u)^T] - \frac{2}{3}\mu(\nabla \cdot u)I \tag{2}$$

where μ is the dynamic viscosity.

2.2 URANS

The URANS method is used in the first part of this study (Paper I). The flow is incompressible. The turbulence is modelled using the k-ω shear-stress transport (SST) model. The segregated flow solver is used to solve the discretized equations. The pressure-velocity coupling approach is adopted for the SIMPLEC (Semi-Implicit Method for Pressure-Linked Equations-Consistent) algorithm. A bounded second-order implicit method is used to discretize the time derivative. The simulations are performed using the software ANSYS Fluent [28].

2.3 IDDES

The turbulence is simulated using the IDDES [29]method in this study, the simulations are performed using the software STAR-CCM+ [24]. The IDDES is combined with the k-ω SST turbulence model. This setup has been tested in several studies on rotating machinery [30, 31]. The IDDES modifies the dissipation in the transport equation of the turbulence kinetic energy k by introducing a hybrid length scale

$$\tilde{l}_{DDES} = \tilde{f}_d(1 + f_e)l_{RANS} + (1 - \tilde{f}_d)l_{LES} \tag{3}$$

where l_{RANS} and l_{LES} are the Reynolds-averaged Navier-Stokes equations (RANS) and LES length scales, respectively. The $\tilde{f}_d$ function blends between RANS and LES and the $\tilde{f}_e$ function slightly enhances the RANS content in the RANS region and they are formulated as

$$\tilde{f}_d = \max\{\tanh(C_{dt}r_{dt})^3, \min[2\exp(-9\alpha^2), 1]\},$$
$$\alpha = 0.25 - d_w/h_{max} \tag{4}$$

where d_w denotes the distance to the wall, and h_{max} is the maximum local grid spacing. The parameter r_{dt} is defined as

$$r_{dt} = \mu_\tau/(\rho\sqrt{\nabla \boldsymbol{u}:\nabla \boldsymbol{u}^T}\kappa^2 d_w^2) \tag{5}$$

where μ_τ is the turbulent eddy viscosity, and the von Karman constant $\kappa = 0.41$. The formulation of f_e reads

$$f_e = max[(f_{e1} - 1), 0]\psi f_{e2} \tag{6}$$

10

where ψ is a low-Reynolds correction that rectifies the activated low-Reynolds number terms of the background RANS model in LES mode [32] The parameters in Eq. 6 reads

$$f_{e1} = \begin{cases} 2\exp(-11.09\alpha^2), & \text{for } \alpha \geq 0 \\ 2\exp(-9\alpha^2), & \text{for } \alpha < 0, \end{cases}$$

$$f_{e2} = 1 - \max[\tanh(C_t^2 r_{dt})^3, \tanh(C_l^2 r_{dl})^{10}],$$

$$r_{dl} = \mu/(\rho\sqrt{\nabla\boldsymbol{u}:\nabla\boldsymbol{u}^T}\kappa^2 d_w^2) \tag{7}$$

The coefficients of the IDDES model adopts the default values in the software STAR-CCM+, i.e. $C_{DES,k-\omega} = 0.78, C_{DES,k-\varepsilon} = 0.61, C_{dt} = 20, C_l = 5$, and $C_t = 1.87$ [24]. The notation of the coefficients is the same as in the software user guide [24]. The wall-normal sizes of the first layer cells near all walls fulfill $\Delta y^+ < 1$.

2.4 FW-H equation

A hybrid approach is adopted to predict the noise generated from the flow. In this approach, the IDDES is coupled with Formulation 1A of Farassat [33]. The ambient air density is set to $\rho_0 = 1.225$ kg/m^3, and the speed of sound $c_0 = 340$ m/s. The Formuation 1A reads

$$p'(\boldsymbol{x},t) = \frac{1}{4\pi}\int_{f=0}\left\{\frac{1}{1-M_r}\frac{\partial}{\partial\tau}\left[\frac{\rho_0 v_n}{r(1-M_r)} + \frac{p\,cos\theta}{c_0 r(1-M_r)}\right]\right\}_{\tau_e} dS$$

$$+ \frac{1}{4\pi}\int_{f=0}\left[\frac{p\,cos\theta}{r^2(1-M_r)}\right]_{\tau_e} dS \tag{8}$$

where $r = |\boldsymbol{x}-\boldsymbol{y}|$, and $M_r = (\boldsymbol{x}-\boldsymbol{y})\cdot\boldsymbol{v}/(rc_0)$. The variable v_n is the local surface normal velocity, and τ_e denotes the emission time. Besides, $cos\theta = (\boldsymbol{x}-\boldsymbol{y})\cdot\boldsymbol{n}$, where $\boldsymbol{n}$ is the unit vector normal to the surface.

According to Neise [34], the fan noise generation at low Mach numbers is dominated by dipole noise sources that are derived based on the FW-H equation. Hence, the noise prediction in this study considers only an impermeable integral surface for Formulation 1A. The integral surface consists of the fan blades, shroud, and backplate (see Figure 1a), this approach is chosen so that the sources for the BPF can be compared. This method agreed well in [35] where the unsteady flow in a centrifugal fan was studied and evaluated with experiments. The upstream and downstream ducts, as well as the fan inlet duct, are neglected. This treatment disregards the acoustic reflection from the duct walls to resemble the conditions in the experimental rig.

11

2.5 Direct Noise Computational (DNC)

2.6 Local mesh refinement

In Paper II, a local mesh refinement study was performed inside the fan at the regions extending from the gap to the blade leading edge (BLE) and along the blade to the blade trailing edge. Here high TKE was found due to gap turbulence in Paper I. These mesh refinement regions (blue) are illustrated in Figure 9. The mesh parameters are listed in Table 2. The refined mesh resolution enables the LES mode for the IDDES, which is controlled by $\tilde{f}_d$ in Eq. 4. $\tilde{f}_d$ blends between the URNAS and LES mode, which depends on the grid spacing and the wall distance.

The mesh size in the upstream duct and downstream duct is 55 cells per meter. According to [24] it should be at least 20 cells per wavelength for the shortest wavelength. This corresponds to a minimum frequency of 124 Hz for this mesh, which is well below the tonal noise at the $BPF = 326.7$ Hz.
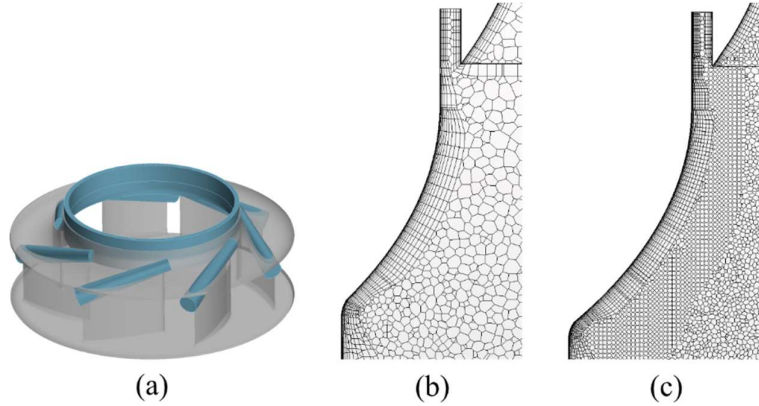

Figure. 9. a) Mesh refinement regions (blue) at the inlet gap and blades top region. Mesh cells near the inlet gap in b) the Coarse-mesh and c) the Refined-mesh.

Table 3. The mesh parameters.

	Coarse-mesh	Refined-mesh	Less-refined[†]	Ultra-refined[†]
Refinement factor	-	1	0.85	1.15
Total number of cells	32×10^6	52×10^6	46.5×10^6	58.3×10^6
Number of cells in the rotating zone	22.9×10^6	41.9×10^6	36.4×10^6	48.2×10^6
Maximum Δy^+ near blade walls	0.93	0.73	0.83	0.65
Cell growth ratio	1.05	1.05	1.05	1.05

† The less-/ultra-refined meshes are generated by adjusting the cell sizes of the refined mesh in the rotating zone.

Important physical quantities describing the fan performance are the static pressure rise, which is between the fan inlet and outlet, and the fan torque. These two quantities from the four cases are listed in Table V. The results of Refined-mesh and Ultra-refined agree well with the experimental data.

The comparison of Refined-mesh, Less-refined[†], and Ultra-refined shows that the mesh refinement in the rotating zone leads to converged results.

Table 4. Fan performance data.

	Static pressure rise (Pa)	Torque (N·m)
Coarse mesh	255.61	1.133
Refined-mesh	267.82	1.127
Less-refined[†]	262.12	1.129
Ultra-refined[†]	267.91	1.127
Experiment	269.65	1.125

The contours of vorticity magnitudes $\|\vec{\omega}\|$ near the fan inlet gap are shown in Figure 10. In contrast to the Coarse-mesh, the Refined-mesh resolves turbulent vortices that originate from the gap. The reason is that the fine mesh resolution turns on the LES mode of the IDDES [35]. The gap turbulence is mixed with the main flow as it is swept downstream. For the sake of brevity, Refined-mesh is chosen for the analysis and discussion hereafter.
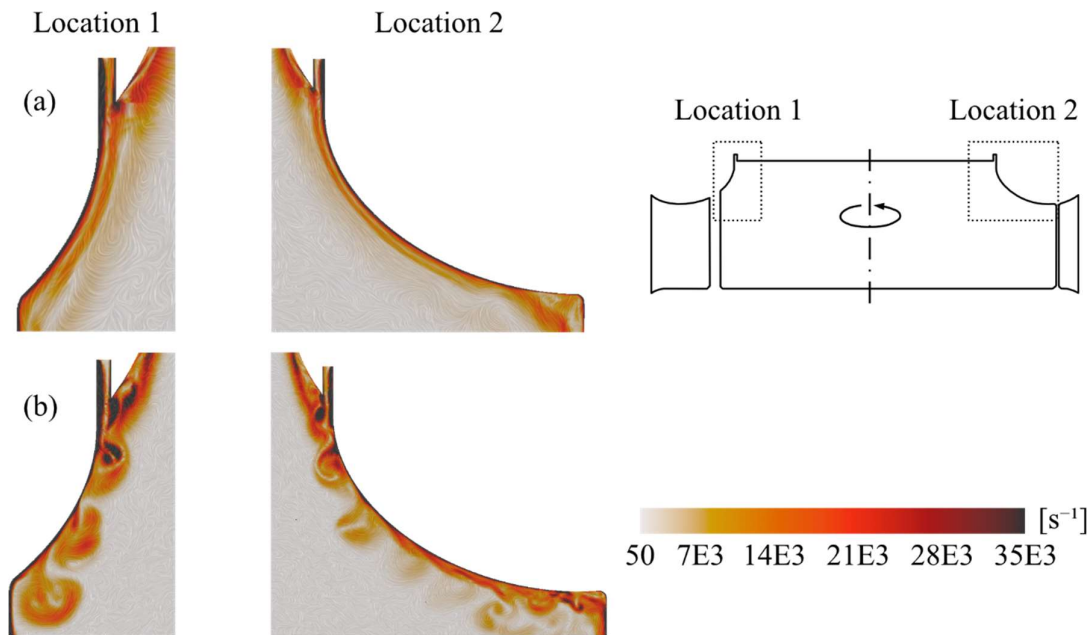

Figure. 10. Instantaneous vorticity magnitudes near the inlet gap. a) Coarse-mesh; b) Refined-mesh.

13

3 Results

3.1 Gap flow (Paper I)

The fan performance is influenced by the flow separation on the blades. The separation is identified based on wall shear stress. Figure 11 shows that there is recirculating flow between the blade and the shroud. Low wall shear stress is observed near the blade trailing edge. Furthermore, it is found that the recirculating flow originates from the fan gap, as illustrated in Figure 12.
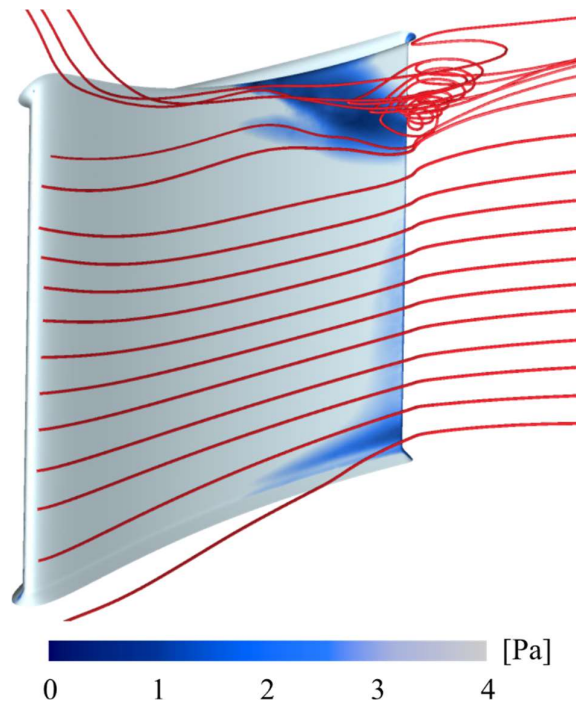

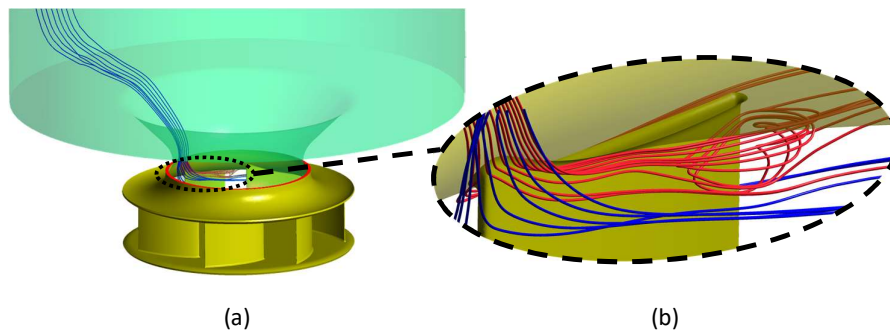Figure 11. Contour plot of the wall shear stress at the blade with airflow visualized with streamlines

Figure 12. Streamlines starting from the inlet (blue) and the gap (red). The gap is shown in Figure 1. a) The fan and inlet duct, b) A magnified view of the blade and shroud intersection.

14

The Power Spectral Density (PSD) of the noise at the microphones, M1 and M2 are shown in Figure 13. The tones measured at M1 agree well with the experimental result. At M2, the tones do not agree well. The noise characteristic can be affected by the flow through the fan [10, 36].

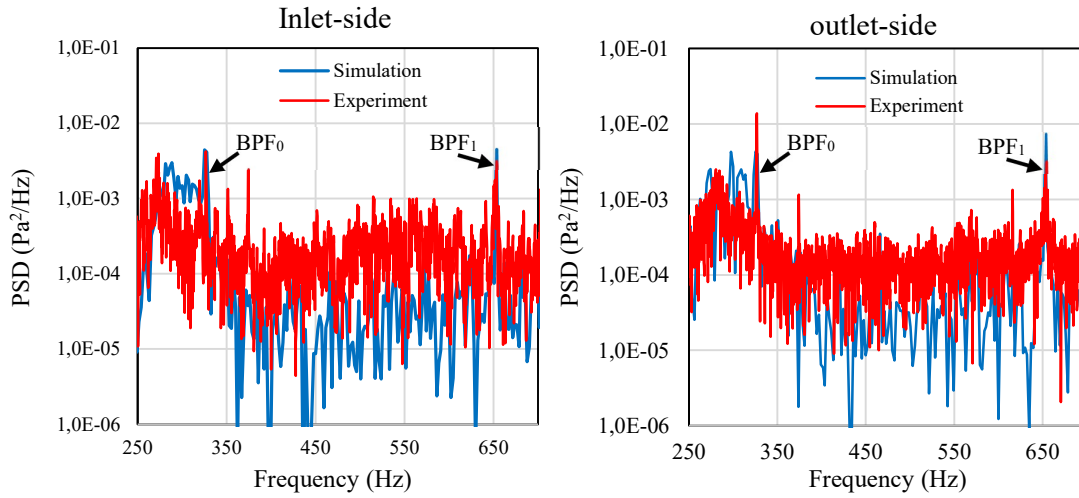Figure 13. Comparison of PDS at the inlet-side (M1) and outlet-side (M2).

3.2 Turbulence from inlet gap (Paper II and Paper III)

Compared with the mesh used in Paper I, the mesh is refined in all regions and especially in the gap and the blade regions. Turbulence develops from the gap between the rotating fan and the stationary inlet duct, as indicated by visualizing vorticity magnitudes near the gap in Figure 14.
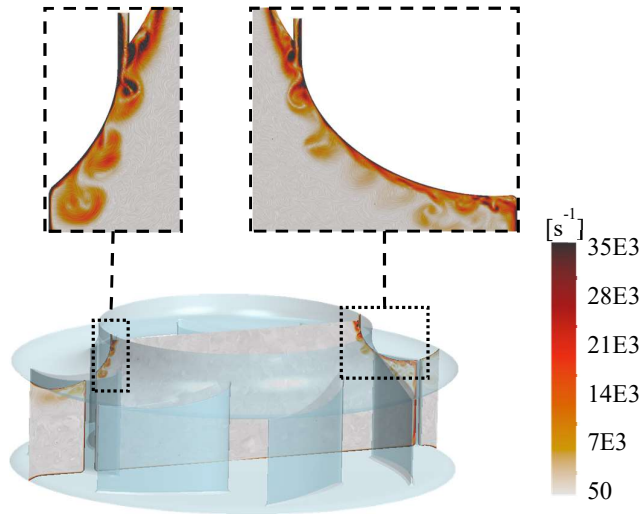
Figure 14. Instantaneous vorticity magnitude near the inlet gap.

The contours of vorticity magnitudes $\|\vec{\omega}\|$ at the blade leading edge for Case 1 is shown in Figure 15a. There are regions with high vorticity magnitude close to the shroud. They are generated when the gap flow is mixed with the main flow. This phenomenon was also observed in previous studies [14]. The black dashed line is a monitoring line positioned at the BLE which extends from the backplate to the shroud. The line follows the blade rotation and the surface pressure is monitored during 12 fan revolutions. The root mean square (RMS) of the surface pressure is shown in Figure 15b. At the position nearest the shroud, the RMS has its highest value. As the distance to the shroud increases, the RMS pressure decays. At the backplate, the RMS pressure is 160 Pa, which is approximately 25% of the value at the shroud (700 Pa).
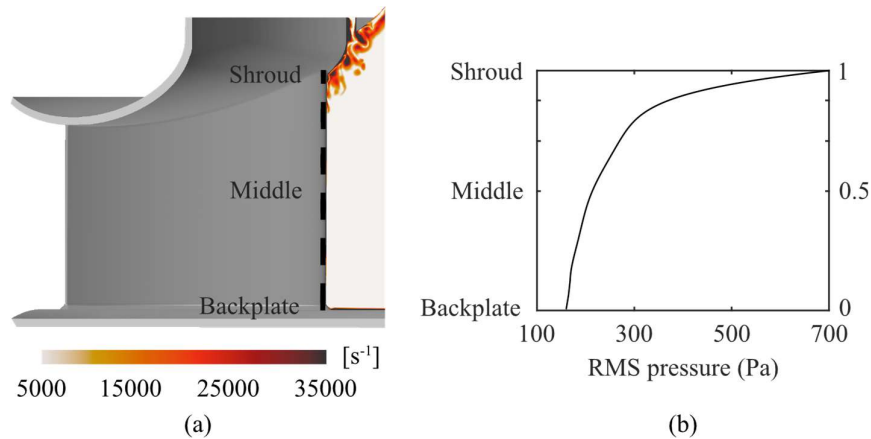

Figure 15. a) Vorticity magnitude $\|\vec{\omega}\|$ at one blade. The black dashed line marks the monitoring line at the BLE; b) the RMS of the pressure fluctuations with respect to the normalized length along the monitoring line

16

The time history of the surface pressure at the monitoring line are shown in Figure 16. At the position shroud, the pressure fluctuates with large amplitudes and high frequencies. As the distance from the shroud increases the amplitudes of pressure fluctuations decrease. Small fluctuations are observed at the middle position. At the backplate, fluctuations are almost negligible.

Moreover, a periodic low-frequency fluctuation in relation to the fan revolution is observed. By comparing the three monitoring points, high-frequency fluctuations decay rapidly with increased distance to the shroud. The periodic low frequency is predominant at the middle position and at the backplate.
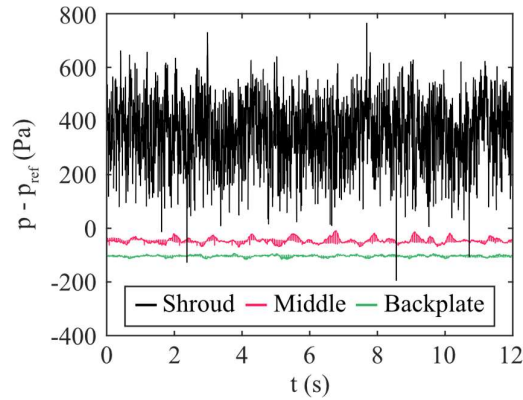
Figure 16. The time history of surface pressure fluctuations at three locations along the BLE

Based on the band filtered PSD of the wall pressure fluctuations, it is possible to find the noise sources. The surface pressure levels (SPL) at the tonal frequencies, $273\ Hz$, $326.7\ Hz\ (BPF_0)$, and $653.3\ Hz\ (BPF_1)$ are illustrated in Figure 17. The highest PSD at all tonal frequencies are located at the blade leading edge close to the shroud.

17

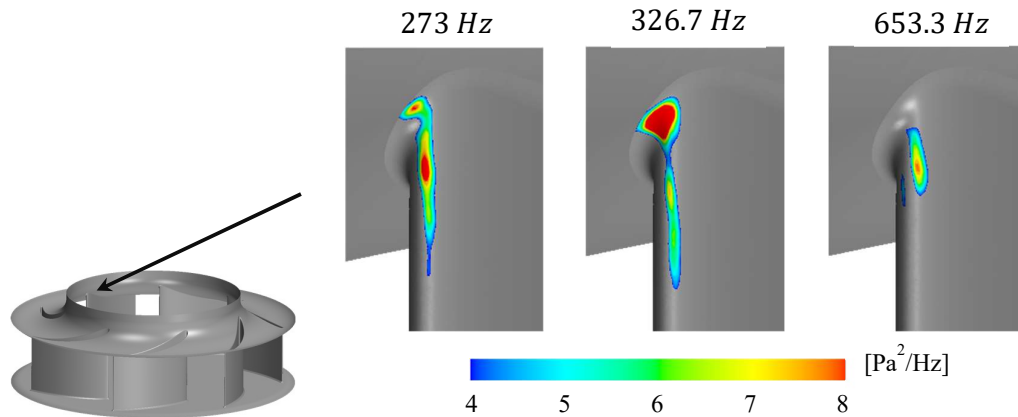273 Hz   326.7 Hz   653.3 Hz

$[Pa^2/Hz]$

4   5   6   7   8

Figure. 17. SPL of the surface pressure fluctuations at three tonal frequencies.

3.3 Inlet gap effect on aerodynamics (Paper III and Paper IV)

The fan performance is compared for the different gap design cases described in Figure 7. The static pressure excluding the reference pressure ($p_{ref} = 101325$ Pa) is displayed along the axial symmetric line for all cases in Figure 18. All cases show consistent pressure amplitudes in the upstream duct of the fan, while differences are seen downstream. The difference in pressure rise downstream of the fan is only due to the gap design. Compared to Case 1, the gap width is larger in Case 2 and smaller in Case 3. Among these three cases, the pressure rise is smallest in Case 2 and largest in Case 3. Therefore, increasing the gap width worsens the fan performance. However, the anomaly is found in Case 4. This case produces larger pressure rise than Cases 1-3, even though its gap width is the same as Case 1. The geometric differences between Cases 1 and 4 are that the gap of Case 4 has a longer streamwise length and a curved shape. These geometric changes lead to an increase in the pressure rise.
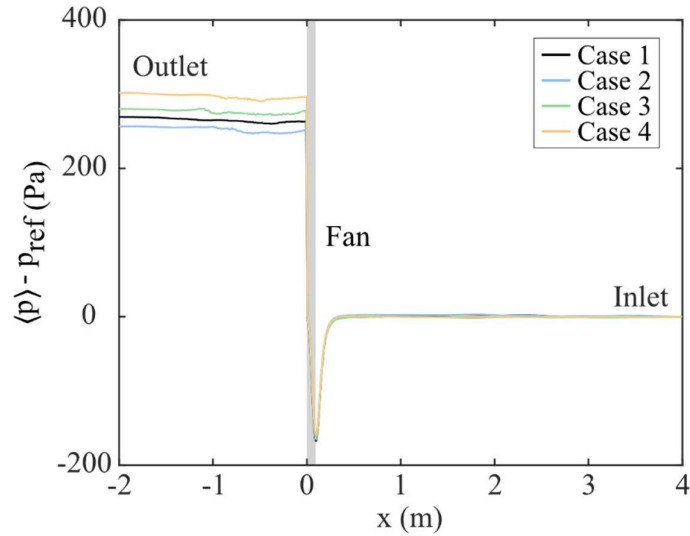
Figure 18. The pressure along the axial axis of the fan across the computational domain. x = −2 corresponds to the location near the outlet and x = 4 near the inlet. The fan location is marked out with the gray zone.

Figure 19 shows the instantaneous pressure in a plane i.e. approximately the midspan of the blades (see Figure 15). The pressure increase in the channel between two neighboring blades is largest in Case 4. This also demonstrates the phenomenon observed in Figure 18 that the pressure at the fan outlet is highest in Case 4. Unlike from Case 4, there are significant pressure fluctuations near the blade trailing edge in Cases 1-3. It is known that the fluctuating pressure distribution is caused by turbulent structures in the flow and affects the fan performance.
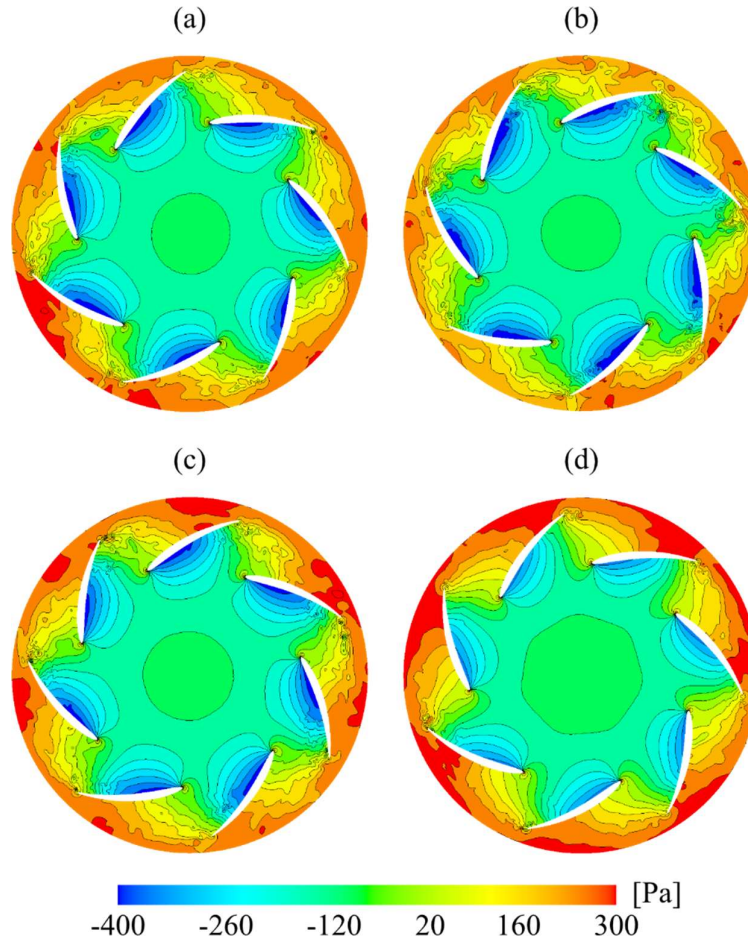
Figure 19. The instantaneous pressure in Plane 3: a) Case 1, b) Case 2, c) Case 3, and d) Case 4.

3.4 Inlet gap effect on turbulence (Paper III and Paper IV)

The RMS pressures at the monitoring line at the BLE are illustrated for all cases in Figure 20a. The line follows the blade rotation and the surface pressure is monitored during 12 fan revolutions. At the position nearest the shroud (Plane 1), the highest RMS pressure is observed for all cases. The RMS pressures have the same physical behavior for all four cases and when the distance to the shroud increases, the RMS pressure decays. From Plane 1 to the backplate, Case 2 has the lowest RMS pressure, and Case 4 the highest. At the backplate, Case 4 has the highest RMS pressure, and the other cases have almost the same.

The time-averaged of the surface pressures at the BLE are shown at different positions for all cases in Figure 20b. The maximum values for all cases occur at Plane 1 (shroud), whereas at the backplate the values are negative. The amplitudes of the maximum and minimum pressure (error bar) are largest at Plane 1 and they decay when the distance from the shroud increases, for all cases. At Plane 1, Case 4 has the highest amplitude. Case 2 has the lowest amplitudes at all positions. At Plane 2 and 3, the maximum positive fluctuations are larger

than the magnitude of the negative ones, and it is the same for all cases. It is clear that Case 2 has the smallest pressure fluctuations at the BLE.
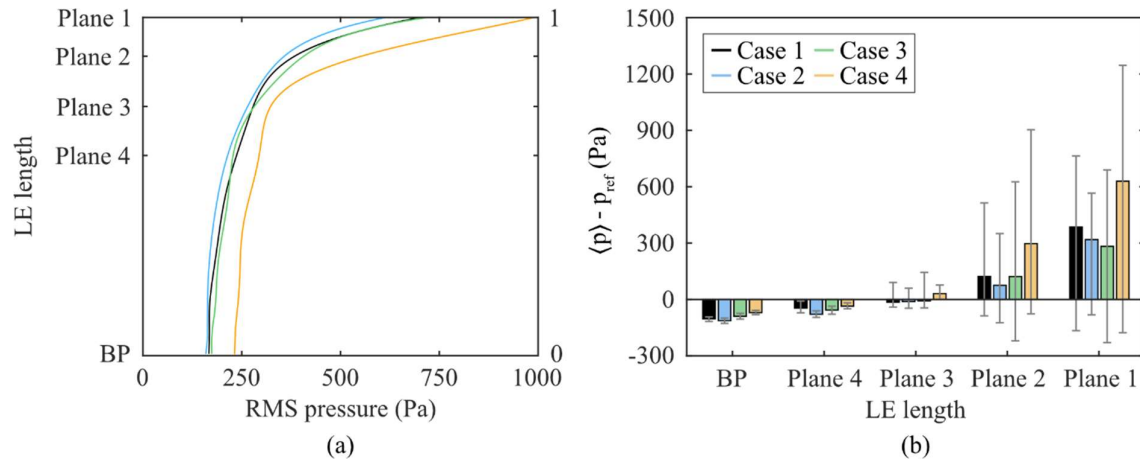

Figure 20. a) The RMS values of the pressure fluctuations for 12 fan revolutions, on one blade at the monitoring line, i.e. BLE; b) the time-average pressure and error bars showing the minimum and maximum pressure. Here, BP corresponds to the backplate.

In the previous Figure 13, it was shown that the PSD of the noise at the tonal frequency, BPF, was in closer agreement upstream of the fan (M1) than downstream (M2). The SPL of the noise at the microphone M1 is compared in Figure 21. The highest BPF amplitude is observed for Case 4, which is 4 dB higher than Case 1. Comparing Cases 1-3 where only the gap width is changed, Case 2 with the largest gap width has the lowest BPF magnitude, and Case 1 with the medium gap width has the medium BPF magnitude. This indicates that increasing the gap width leads to a reduction in the tonal noise generation. Moreover, a similar trend is observed for the broadband noise, i.e., magnitudes increase sequentially in Case 2, Case 3, and Case 1. In contrast to Cases 1-3, Case 4 produces larger tonal noise at the BPF. The reason for this might be that the longer spacing in the gap in Case 4 triggers more stretched vortices compared with Case 1. These results agree with the results from Figure 20, where Case 2 had the lowest RMS pressure on the BLE.
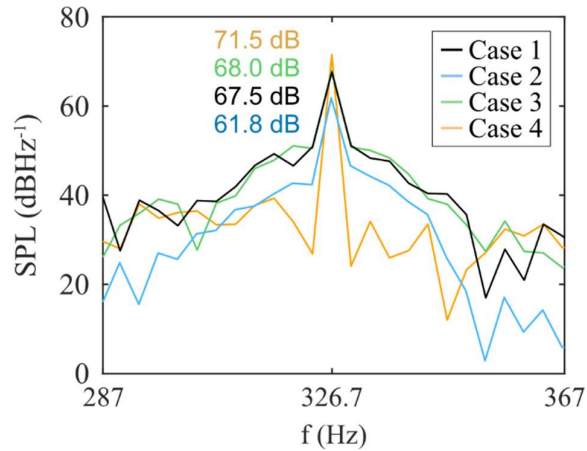
Figure 21. The SPL of the sound pressure at the microphone M1 upstream of the fan. The tonal frequency $BPF = 326.7$ Hz. The SPL values of the tones are presented.

Based on the band-filtered PSD of surface pressure fluctuations, the location and magnitudes of dominant tonal noise sources are evaluated. The results at the tonal frequency of $BPF = 326.7$Hz are illustrated in Figure 22. The location of the highest surface pressure fluctuations is at the same position (the top side of the BLE that is connected to the shroud) for all cases. Besides, this position is found with high RMS pressure. The differences between the Cases are the maximum magnitude and the size of the high-magnitude region. Case 4 has the largest sound pressure (see Figure 21), and it has also the largest area and magnitude at the tonal frequency. The high energy locations are consistent with the RMS pressure fluctuations indicated in Figure 20.

Additionally, in Cases 1, 2, and 3, small magnitudes are seen at the blade trailing edge close to the shroud. In contrast, Case 4 does not show such a region. This agrees with the findings in Figure 19, where surface pressure fluctuations were found at the same location for Cases 1, 2, and 3 but not for Case 4.
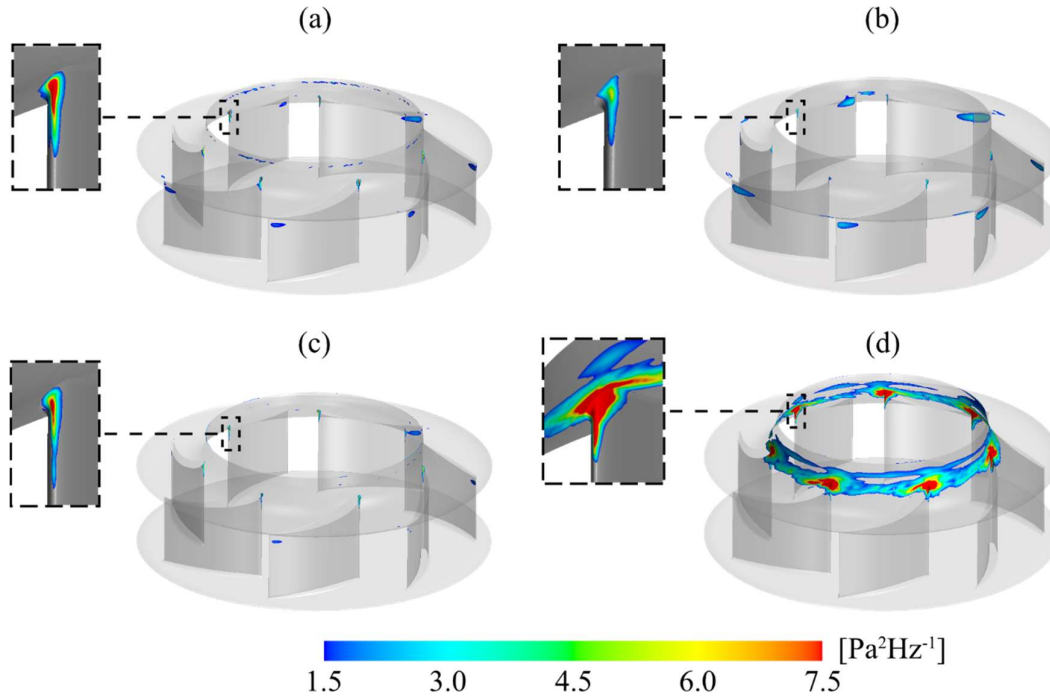
Figure 22. The PSD of surface pressure fluctuations at $BPF = 326.7$ Hz. a) Case 1, b) Case 2, c) Case 3, and d) Case 4.

3.5 Low-frequency rotation influences of inlet gap (Paper V)

A snapshot of isosurfaces of $p = 340 \; Pa$ and contours of the velocity magnitudes at the gap is illustrated in Figure 23a. Note that in the fan passages, $340 \; Pa$ is comparatively high pressure. As seen in the figure, regions of high pressure (colored orange) are found at the pressure side of Blades 2 and 3 close to the BTE. The high pressure is unevenly distributed among the fan passages. The velocity magnitudes are also unevenly distributed at the gap, where clear low and high-velocity regions are indicated.

Figure 23b shows the high-pressure regions of $p = 340 \; Pa$, streamlines of the velocity magnitudes, and the velocity magnitudes at the gap. There are regions with high pressure at Blade 2. The streamlines from the gap show that the pressure region is formed by the flow through the low-velocity magnitude region at the gap. At the same time, there are no regions with high pressure at Blade 6. At this blade, the streamlines from the gap follow Blade 6 and shroud intersection smoothly. The turbulence initialized at the gap affects the flow at the blade and shroud intersection on the pressure side of the blades.
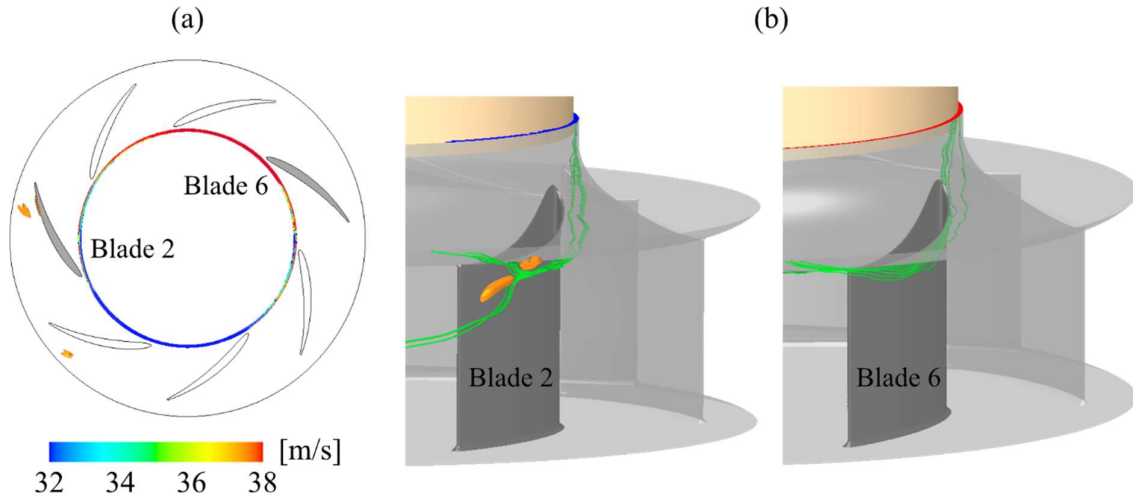
Figure 23. Iso-surface of $p = 340\ Pa$ colored orange, and contours of a) the velocity magnitudes at the gap. b) Streamlines from the gap at Blades 2 and 6, and contours of the velocity magnitudes at the gap.

A monitor point, P1, is set to observe pressure, as shown in Figure 24a. P1 is located on Plane 3, i.e. approximately the midspan of the blades. The time history of the pressure p at P1 is displayed in Figure 24b. P1 follow the fan rotation and the time history is shown over 25T, where T = 0.0214 s is one fan rotation period. The curves are fitted with the Gaussian function with a smoothing factor of 0.87 and are colored in red. A low-frequency fluctuation is found with a time period of 0.43 s. It indicate that a low-frequency rotation in relation to the fan rotation takes place in the fan and that the period time is approximately 0.43 s ≈ 20T.
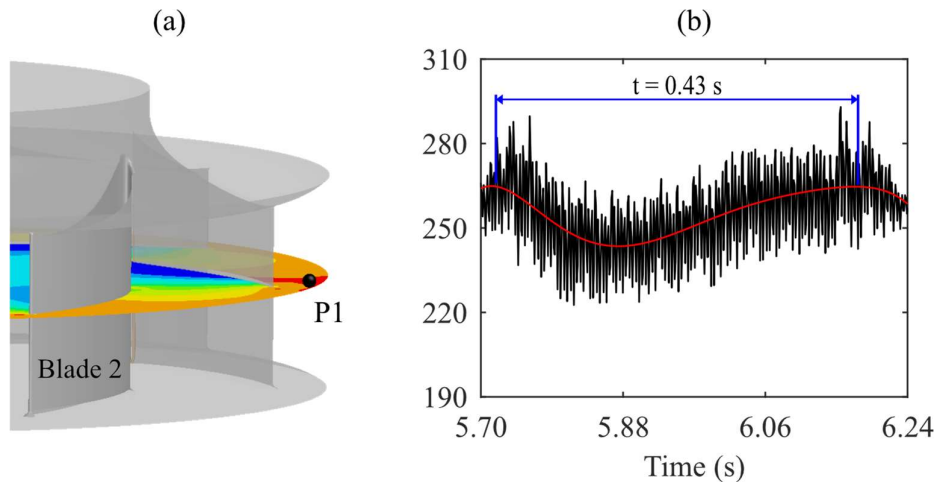

Figure 24. a) Monitor point P1. b) The time history of the pressure p in P1. The red lines are curve fitted to the instantaneous pressure.

24

Figure 25 illustrates snapshots of the velocity magnitudes at the gap, the pressure p in Plane 2, and the surface pressure on Blade 3. Here, Blade 3 is colored black to illustrate the blade position. There are regions with low-velocity magnitudes at the gap, high-pressure regions in Plane 3, and regions with high surface pressure on Blade 3, which move with the same angular speed. This region appears at the same position, at t_0 and $t_0 + 20T$, which supports the finding in Figure 24b.

The regions with high pressure always occur at the same circumferential position as the regions with low-velocity magnitudes. This phenomenon can be explained based on high turbulence regions and streamlines illustrated in Figures 23. The flow through the gap causes turbulent flow structures which are unevenly distributed among the blades. Regions with high pressure always occur at the blades where the flow is highly turbulent. It is concluded that the region of high pressure is connected to large turbulent structures caused by the low-velocity region at the gap.
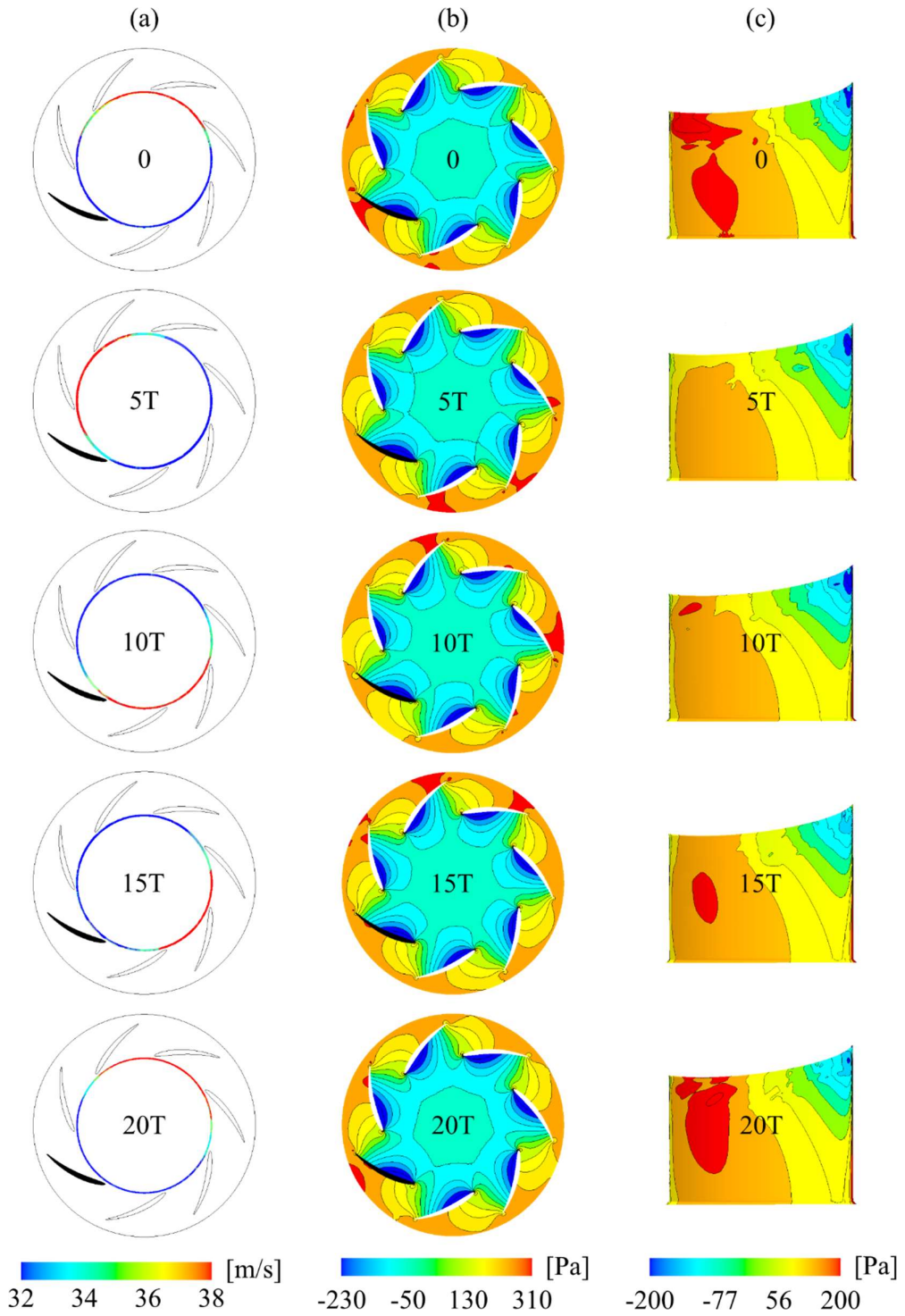
Figure 25. Snapshots of a) velocity magnitudes at the gap, b) the pressure p in Plane 2, and c) Snapshots of the surface pressure p on Blade 3. The blade colored black displays Blade 3.

4 Conclusion

Flow recirculation is found at the suction side of the blade close to the shroud. It is associated with the gap between the shroud and the inlet duct. The recirculating flow can influence the fan efficiency and generate tonal noise.

Different pressure distributions among the blades are found and ascribed to the turbulence originating from the inlet gap. The turbulence develops along the shroud wall and interacts with the blades at the BLE. The interaction renders the uneven surface pressure distributions among the blades as well as the significant peak differences. The peak values are related to the intensive levels of the resolved turbulence. As the distances to the inlet gap and the shroud increases, the difference of the pressure distributions among the blades decays. The reason is that the resolved turbulence from the inlet primitively develops along the shroud. The influence of the turbulence on the blades is, therefore, effective near the shroud.

The wall-pressure fluctuations indicates that the locations of the tonal noise sources $273\ Hz$, BPF_0 and BPF_1 agree with the locations of the uneven surface pressure distributions and the significant pressure peaks, which are near the blade leading edges.

The gap design affects the aerodynamic performance and the acoustic emission in a clear contradiction. The pressure rise decreases from Case 4, Case 3, Case 1 to Case 2. However, the noise is reduced in the reverse order: Case 2, Case 1, Case 3 and Case 4. For Case 4 exhibiting the largest pressure rise, vortices are less intensive near the BTE well inside the blade passage, and at the same position, there are less pressure fluctuations. Thus, the aerodynamic performance is related to the turbulence inside the blade passage. However, Case 4 is the worst acoustic case. This is attributed to the strongest gap turbulence near the wall at the BLE. The turbulence from the gap is ingested into the blade passage and results in the strongest pressure fluctuations. The synthesis of these effects suggests the physical mechanisms that given the turbulence at the entry becomes stronger, the flow inside the blade passage is stabilized. Consequently, the fluctuations near the BTE are mitigated, resulting in improved aerodynamic performance.

Unevenly distributed regions with high pressure are found at the pressure side of the blades close to the shroud. The velocity magnitudes at the gap are also unevenly distributed, where clear low and high-velocity regions are indicated. A correlation between the high-pressure and the low-velocity magnitudes is observed, that is, the high-pressure regions occur downstream of the region of the low-velocity magnitude. Intensive turbulent flow structures are developed from the low-velocity region and are swept along the intersection between the blade and

shroud, on the pressure side of the blade. Eventually, the turbulence gives rise to a high-pressure region near the BTE. This unsteady flow behavior revolves around the fan rotation axis. And its period is 5% of the fan rotation speed, based on the analysis of the time history of the gap velocity magnitudes and the evolution of the high-pressure region. The same frequency of the high pressure was also found in previous experimental measurements

Reference

[1] T. Roberts, "We Spend 90% of Our Time Indoors. Says Who?," Retrieved from https://www.buildinggreen.com/blog/we-spend-90-our-time-indoors-says-who, (2016).

[2] B. Berglund, T. Lindvall, and D. Schwela, "New Guidelines for Community Noise," Noise & Vibration Worldwide **31**, 24-29 (2000).

[3] M. Azimi, "Noise Reduction in Buildings Using Sound Absorbing Materials," Journal of Architectural Engineering Technology **6,** (2017).

[4] J. Seabi, K. Cockcroft, P. Goldschagg, and M. Greyling, "A prospective follow-up study of the effects of chronic aircraft noise exposure on learners' reading and comprehension in South Africa" Journal of Exposure Science and Environmental Epidemiology **25**, (2015).

[5] M. Klatte, K. Bergstrom, and T. Lachmann, "Does noise affect learning? A short review on noise effets on cognitive performance in children" Frontiers in Psychology **4**, (2013).

[6] L.M. Wang and C.C. Novak, "Human performance and perception-based evaluations of indoor noise criteria for rating mechanical system noise with time-varying fluctuations," ASHRAE Transaction **116,** 553-568 (2010).

[7] V. Pommier-Budinger and O. Cherrier, "Baffle silencer with tunable resonators for adaptive control of variable tonal noise," Journal of Vibration and Control **21,** 1801-1809 (2015).

[8] J.E. Ffowcs Williams and D.L. Hawkings, "Theory relating to the noise of rotating machinery," Journal of Sound and Vibration **10,** 10-21 (1969).

[9] D. Wolfram and T.H. Carolus, "Experimental and numerical investigation of the unsteady flow field and tone generation in an isolated centrifugal fan impeller," Journal of Sound and Vibrations **329,** 4380-4397 (2010).

[10] M. Sanjose and S. Moreau, "Direct noise prediction and control of an installed large low-speed radial fan," European Journal of Mechanics **61,** 235-243 (2017).

[11] F. Pérot F, M.S. Kim, V.L. Goff, X. Carniel, Y. Goth Y, and C. Chassaignon, "Numerical optimization of the tonal noise of a backward centrifugal fan using a flow obstruction," Noise Control Engineering Journal **61,** 307-319 (2013).

[12] J.S. Choi, D.K. McLaughlin, and D.E Thompson, "Experiments on the unsteady flow field and noise generation in a centrifugal pump impeller," Journal of Sound and Vibration **263,** 493-514 (2003).

[13] C. Hariharan and M. Govardhan, "Effect of inlet clearance on the aerodynamic performance of a centrifugal blower," International Journal of Turbo and Jet Engines **33**, 215-228 (2016).

[14] Y. Lee, "Impact of fan gap flow on the centrifugal impeller aerodynamics," Journal of Fluids Engineering **132**, 1-9 (2010).

[15] Y. Lee, V. Ahuja, A. Hosangadi, and R. Birkbeck, "Impeller Design of a Centrifugal Fan with Blade Optimization," International Journal of Rotating Machinery (2011).

[16] M. Ubaldi, P. Zunino, and A. Cattanei, "Relative Flow and Turbulence measurements Downstream of a Backward Centrifugal Impeller," Journal of Turbomachinery **115**, 543-551 (1992).

[17] M.W. Johnson and J. Moore, "The Development of wake flow in a Centrifugal Impeller," Journal of Engineering for Power **102**, 382-389 (1980).

[18] L. Mongeau, D. Thompson, and D. McLaughlin, "Sound generation by rotating stall in centrifugal turbomachines," Journal of Sound and Vibration **163**, 1-30 (1993).

[19] Y.H. Yu, "Rotor blade-vortex interaction noise," Progress in Aerospace Sciences **36**, 97-115 (2000).

[20] R. Schaefer and M. Boehle, "Influence of the mesh size on the Aerodynamic and Aeroacoustics of a Centrifugal Fan using Lattice-Boltzmann Method," 23rd International Congress on Acoustics in Aachen 1882-1889 (2019).

[21] Tautz M. Aeroacoustic Noise Prediction of Automotive HVAC System. FAU Forschungen, Reihre B, Medizin, Naturwissenschaft, Technik Band 27. Erlangen: FAU University Press 2019.

[22] Jones W. P. Air conditioning applications and design. 2 ed. Arnold 1997:294-295.

[23] Lighthill M.J. On Sound Generated Aerodynamically. I General Theory. Proc. R. Soc. Lond. A 1952;211:564-587.

[24] Siemens PLM Software. STAR-CCM+ User Guide (Version 12.04) 2017.

[25] P. Spalart, S. Deck, M. Shur, K. Squires, M. Strelets, and A. Travin, "A new version of detached-eddy simulation, resistant to ambiguous grid densities," Theoret. Comput. Fluid Dynamics 20, 181-195 (2006).

[26] J.H. Ferziger and M. Peric, "Computational Methods for Fluid Dynamics," 3rd rev. ed., Springer-Verlag, Berlin (2002).

[27] H.-D. Yao andL. Davidsson, "Vibro-acoustics response of simplified glass window excited by the turbulent wake of a quarter-spherocylinder body," The Journal of the Acoustical Society of America 146, 3163-3176 (2019).

[28] Ansys Inc. Fluent User Guide (Version 19.0) 2018.

[29] M.L. Shur, P.R. Spalart, M.K. Strelets, and A.K. Travin, "A hybrid RANS-LES approach with delayed-DES and wall-modelled LES capabilities," Int. J. Heat Fluids Flow 29, 1638-1649 (2008).

[30] A. Rynell, G. Efraimsson, M. Chevalier, and M. Åbom, "Inclusion of upstream turbulent inflow statistics to numerically acquire proper fan noise characteristics," SAE Technical Paper 2016-01-1811 (2016).

[31] A. Rynell, M. Chevalier, M. Åbom, and G. Efraimsson, "A numerical study of noise characteristics originating from a shrouded subsonic automotive fan," Applied Acoustics 140, 110-121 (2018).

[32] K.S. Brentner and F. Farassat, "Analytical comparison of the acoustic analogy and Kirchhoff formulation for moving surfaces," AIAAA J 36, 1379-86 (1998).

[33] W. Neise, "Review of fan noise generation mechanisms and control methods," In: Proceedings of the Fan Noise 1992 International Symposium, Senlis, France. 45-56 (1992).

[34] M. Younsi, F. Bakir, S. Kouidri, and R. Rey "Numerical and experimental study of unsteady flow in a centrifugal fan," In proceedings of the 7th European Turbomachinery Conference, Athens, Greece, 2007, 175-189 (2007).

[35] S. Salunkhe, O.E Fajri, S. Bhushane, D. Thompson, D. O´Dohety, T. O´Dohety, and A. Mason-Jones, "Validation of tidal stream turbine wake predictions and analysis of wake recovery mechanism," Journal of Marine Science and Engineering **7**, (2019).

[36] A. Lawrenson, G. Berg, C. Carlsson, M. Fransson, L. All, inventors; Swegon AB, applicant, "Low profiled AHU with tilted rotary heat exchange," International patent WO 2010085197, (2010)